Nitric Oxide Planar Laser Induced Fluorescence Rotational Thermometry Characterization of a Hypersonic Boundary Layer

Madeline A. Smotzer*
Texas A&M University, College Station, TX, 77845

Zachary D. Buen†
L3Harris, San Leandro, CA, 94577

Casey J. Broslawski‡
NASA Langley Research Center, Hampton, VA, 23681-2199

Ashley N. Moran§, Bryan J. Morreale¶,Simon W. North‖, Rodney D.W. Bowersox**
Texas A&M University, College Station, TX, 77845

Nitric oxide (NO) planar laser-induced fluorescence (PLIF) was performed to determine rotational temperature profiles and fluctuations within a hypersonic boundary layer above the surface of a 2.75° half-angle wedge test article. The experiments were performed in the Texas A&M University Actively Controlled Expansion (ACE) hypersonic blow-down wind tunnel at $M = 5.7$ **and** $Re = 6 \times 10^6/\text{m}$**. The NO was introduced to the flow in the settling chamber of the ACE tunnel and probed using two laser sheets near 226 nm. The resulting NO PLIF fluorescence signal was acquired using in-house software, which simultaneously recorded tunnel conditions. After a Fast Fourier Transform (FFT) blurring and statistical treatment was performed, the preshock temperature was evaluated to be 58 ± 2 K (3.5%), while the turbulent boundary layer temperature near the wall was found to be 350 K with fluctuations on the order of ±25 K (7%). The relative temperature fluctuations were determined to be** $3 - 5\%$ **in the freestream and peaked at 33% in the turbulent boundary layer. The advantages and disadvantages of seeding NO in the tunnel settling chamber for thermometric PLIF measurements are discussed.**

Nomenclature

ACE = Actively Controlled Expansion Tunnel

C_{12} = Correction Constant

*Ph.D. Candidate, Department of Chemistry, AIAA Student Member.
†Optical Engineer.
‡Research Aerospace Engineer, Aerothermodynamics Branch, MS 408A, Young Professional AIAA Member.
§PhD Candidate, Department of Chemistry, AIAA Student Member.
¶Assistant Professor, Department of Aerospace Engineering, AIAA Member.
‖Professor and Department Head, Chemistry Department.
**Professor, Aerospace Engineering; Senior Associate Dean for Research and CRO; Deputy Director, Texas A&M Engineering Experiment Station; Regents Professor; Holder, Ford I Professorship; AIAA Fellow.

C_j = Column Index

C_T = Column Resolution

ΔE = Energy Difference

$\frac{\delta T}{T}$ = Temperature Uncertainty

$\frac{\delta R_{12}}{R_{12}}$ = Fluorescence Ratio Uncertainty

DC = Direct Current

FFT = Fast Fourier Transform

k_B = Boltzmann Constant

LIF = Laser Induced Fluorescence

M = Mach Number

NO = Nitric Oxide

N_2 = Nitrogen

$PLIF$ = Planar Laser Induced Fluorescence

PID = Proportional Integral Derivative

R_i = Row Index

R_T = Row Resolution

Re = Unit Reynolds number (10^6/m)

ROI = Region of Interest

$\frac{S_1}{S_2}$ = Signal Ratio

T_{rot} = Rotational Temperature

T' = Temperature Fluctuations

T = Instantaneous Temperature

$\overline{T}$ = Average Temperature

UV = Ultraviolet

w = User Defined Weighting Factor

X_{ij} = Pixel value

NAL = National Aerothermochemistry and Hypersonics Laboratory

I. Introduction

The boundary layer flow over hypersonic vehicles plays a significant role in their thermal management [1]. Therefore, it is critical to understand the thermal behavior of the air molecules just above the vehicle surface to develop both empirical and computational models. Present and future vehicle designs rely on computational fluid dynamic (CFD)

simulations to predict the evolving boundary layer behavior along the surface. Turbulent boundary layer modeling is inherently difficult due to the statistically fluctuating molecular mass and energy exchange. High fidelity direct numerical simulations (DNS) solve the Navier-Stokes equations to resolve all turbulent scales in space and time without any turbulence closure models to predict boundary layer behavior, however such simulations are not only computationally expensive but impossible for many flow conditions. Several reduced order models have been developed to mitigate the computational demand and have the potential for high throughput analysis. These reduced order turbulence models often contain time- or mass-averaged terms that yield mean and a fluctuating components. Employing the assumptions that the dissipative structures of turbulence below the Kolmogorov length scale are statistically isotropic, and the modeled fluctuating term is calculated with statistical significance, the potential error can be minimized. Additionally, these mean and fluctuating terms are often coupled physical parameters. For example, local internal energy and velocity are coupled, which is demonstrated by the Favre time-averaged transport equation [2–4]. These reduced models rely on empirical databases for validation due to assumptions associated with turbulence; however, current experimental literature needed to validate reduced algebraic turbulence models is limited. Hence, a robust, cohesive empirical database is critical to advance next generation hypersonic turbulence models. Rotational thermometry measurements within a hypersonic boundary layer along a flat plate wedge will expand such a database.

A variety of techniques provide thermal information within a hypersonic flow field. A study performed by Semper and Bowersox [5] indirectly measured the surface normal temperature profile of a laminar boundary layer using cold-wire anemometry coupled with pitot probe measurements [5]. While the study provided a 1-D mean temperature measurement, it is important to note the measurement probes can produce local flow perturbations. In an effort to reduce the flow perturbations, several nonintrusive optical diagnostics have been implemented within hypersonic flow measurements. Infrared (IR) thermography, a common nonintrusive technique, provides the thermal loading a surface experiences under hypersonic conditions. The heat flux maps provided by IR thermography are informative but incapable of contributing insight to off-body flow behavior. Other techniques must be used simultaneously to obtain off-body behavior. For example, Kostak and Bowersox [6] used IR thermography in conjunction with hot-wire measurements to measure surface heat flux maps and off-body measurements on the BOLT model to study flow transition. A technique capable of off-body measurements is Filtered Rayleigh scattering (FRS), which yields gas-phase temperature measurements without the use of tracer gas species. The technique calculates spatially-resolved spectral signatures and thereby absolute temperatures. The collected spectral signature is dependent upon absolute pressure; any fluctuations may introduce error. Additionally, the measurement is averaged over the optical path, so pressure gradients complicate the temperature fitting scheme. A recent study by Feng et al. [7] investigated FRS sensitivity to temperature and pressure. BOXCARS is another spectral technique capable of directly measuring temperature in a range of gaseous flow fields. Variations along the optical axis do not impede the accuracy of this technique due to the geometry of the laser interrogation region. The 1-D output from BOXCARS challenges interpolation into a 2-D temperature profile.

Laser diagnostics have evolved to become key techniques in performing off-body boundary layer measurements due to their nonintrusive nature. One such technique is Planar Laser Induced Fluorescence (PLIF), which captures the resulting fluorescence from exciting a particular tracer species in the flow via a thin laser sheet to produce highly spatially and temporally resolved temperature and density measurements [8, 9]. Nitric oxide (NO) has become a common tracer species for PLIF due to its well characterized fluorescence and thermochemical compatibility with air [10]. PLIF thermometry measurements have been demonstrated in various flow field environments where large temperature gradients occur including combustion, blow-down, and high enthalpy facilities [10, 11]. NO PLIF rotational studies have shown viability in shock tunnels via nascent NO in the flow while studying wedge models with a cold wall [1, 10]. The studies demonstrated the ability to obtain average rotational temperature profiles that agreed well with theoretical profiles [10]. More recently, boundary layer studies conducted in a conventional wind tunnel seeded NO directly into the boundary layer [12, 13]. Several authors have seeded NO into the boundary layer using jets, as well as a slot with a low mass flow rate to increase the NO tracer species concentration in the boundary layer while also minimizing flow perturbation [12, 14, 15]. A benchtop facility constructed to support a series of thermal nonequiliubrium experiments seeded NO into the settling chamber both to support PLIF measurements and to act as a rapid relaxer [16]. The current experiments seed NO prior to flow conditioning and expansion to ensure no perturbation of the boundary layer, full dispersion of the gas through the region of interest, and complete thermalization of the NO with the bath gas, all effects of concern to wall-injected PLIF experiments [17].

In the present study, NO PLIF rotational thermometry was performed in a Mach 5.7 flow over a 2.75° half-angle wedge test article for the first time in the Actively Controlled Expansion (ACE) blow-down wind tunnel facility. The NO molecular tag is seeded into the flow upstream of the expansion. The collected NO fluorescence images were analyzed to produce 2-D temporally and spatially resolved rotational temperature maps. The 2-D rotational temperature maps were further reduced to produce 1-D temperature profiles normal to the surface. Instantaneous and averaged temperature maps with the corresponding profiles will be discussed along with their respective uncertainties. The instantaneous temperature maps permit quantification of the temperature fluctuations within a turbulent boundary layer. It was critical in quantifying the relative uncertainty for the rotational thermometry measurements to define the true turbulent temperature fluctuations. Statistical treatment and image processing algorithms were developed that will be discussed. Temperature measurements were performed at two (upstream and downstream) streamwise locations along the test article to compare initial conditions to the breakdown to turbulence. The average NO PLIF rotational temperature profiles are compared to a US3D computational model [18] for both laminar and turbulent conditions.

II. Methodology

A. Actively Controlled Expansion Tunnel (ACE)

The experiments were performed in the blow-down wind tunnel facility at Texas A&M University's NAL. A detailed description of the design and performance of the facility is in Refs. [19, 20]. The ACE facility is a conventional wind tunnel with a variable Mach number from 5 – 8 and a unit Reynolds number sweep range of 0.5×10^6 m^{-1} to 8×10^6 m^{-1}. A 23.2 m^3 tank is pressurized to 1.723×10^4 kPa with dried air and a Fox Two-Stage Ejector pulls vacuum onto the ACE facility through the diffuser. The nominal run time is 40 s as limited by the ejector requisite mass flow rate of 25 kgs^{-1}. The mass flow rate through the ACE facility is 1.0 – 1.5 kgs^{-1}. The air passes through a Chromalox heater to convectively preheat the ACE facility infrastructure to 430 K to avoid O_2 liquefaction during the expansion. A thermocouple and a pitot probe are used to measure the stagnation conditions within the preexpansion region, i.e., the ACE tunnel settling chamber. Freestream disturbances are reduced through a series of flow conditioners upstream of the converging section of the 2-D symmetric de Laval nozzle. A separate pressure transducer is mounted near the exit of the nozzle to measure the static pressure within the test section. The ACE test section contains multiple optical ports fitted with UV-grade fused silica windows. The laser optics were mounted on a custom-made infrastructure surrounding the ACE tunnel to isolate them from test section vibrations. This infrastructure also allowed for optimal mounting of the ICCD cameras. For boundary layer studies, the test article was left in the tunnel during preheat to prevent misalignment with the laser optics. At Mach 6, the measured RMS fast response pitot probe pressure fluctuations are ∼1% and the RMS Mach number fluctuations are ∼0.5% in the exit plane of the core flow [19, 20]. A diagram of the facility is shown in Figure 1 and a summary of the ACE tunnel conditions selected for the experiment are shown in Table 1.

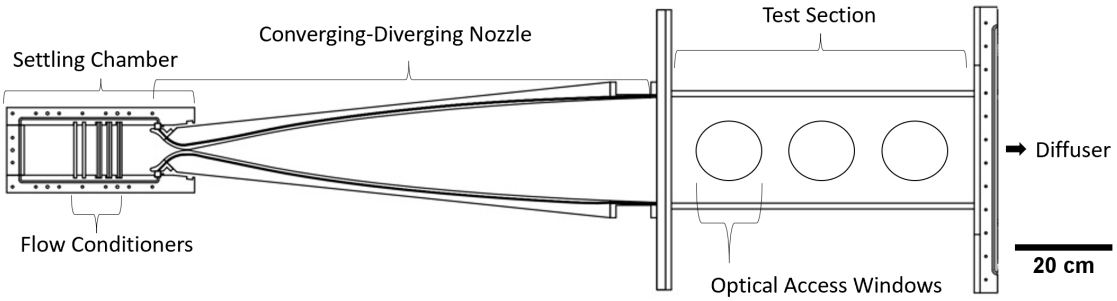

Fig. 1 Diagram of the Actively Controlled Expansion (ACE) blow-down wind tunnel facility. Flow travels from left to right. All measurements were performed in the test section.

Table 1 ACE tunnel conditions.

M	Re $(\times 10^6/m)$	P_0 (kPa)	T_0 (K)	P $(Torr)$	T (K)	ρ $(\frac{kg}{m^3})$
5.70 ± 0.05	6.00 ± 0.25	496.42 ± 20.68	430 ± 15	3.23 ± 0.13	57.35 ± 2.00	2.61 ± 0.002

B. Test Article

The test article used for the NO PLIF rotational thermometry experiments was a 2.75° half-angle wedge. A detailed description of the test article can be found in Refs. [21, 22]. Briefly, the wedge was designed to have a zero-pressure gradient along the length of the plate. An insert with diamond-shaped trip geometries with a height of 2.57 mm and spacing of 6.84 mm between each trip center can be added 6 cm downstream of the leading edge to introduce turbulence to the flow. Directly downstream of the trip insert were two copper electrodes where a 47 W DC glow discharge plasma can be used to generate thermal nonequilibrium, though no plasma was generated for the current work. Two antireflective fused silica window inserts starting 10 and 23.5 cm downstream of the leading edge allowed laser sheets to be passed through the boundary layer and test article with minimal reflections; these windows were 3.8 cm × 6.6 cm and 25.5 cm × 6.6 cm, respectively. Figure 2 shows a cutaway view of the wedge mounted within the ACE tunnel test section. Measurements were made at two locations along the surface of the plate. The upstream location (Location 1), 120 mm from the leading edge, was selected to assess initial conditions and obtain a baseline for laminar and turbulent measurements downstream. The downstream location (Location 2), 405 mm downstream of the leading edge, was selected to allow comparison between the experimental measurements and computations after the simulations were run along the length of the test article; it avoided a known reflected shock identified by schlieren measurements to provide a clean environment for comparison.

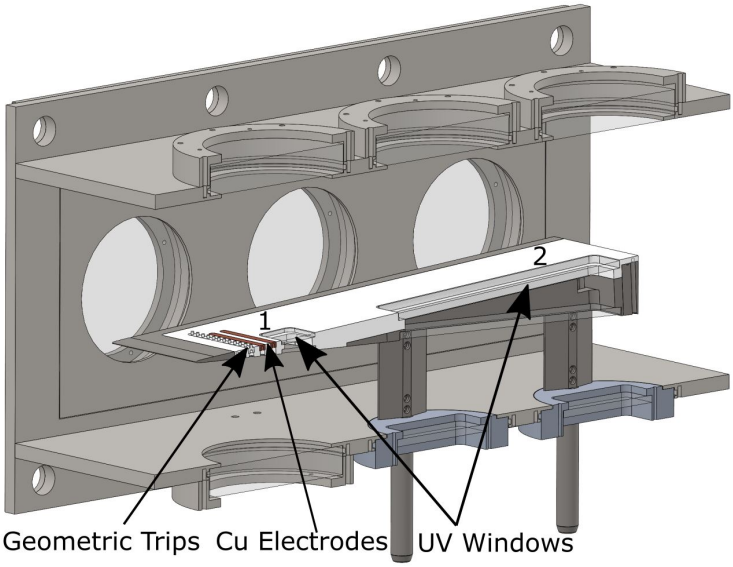

Fig. 2 Half-section view of the test article.

C. US3D Computational Model

Supporting computations for comparison with the experimental data were produced utilizing the US3D Computational Fluid Dynamics (CFD) code [18]. US3D is a high-fidelity computational analysis package designed to model hypersonic

flows with both thermal and chemical nonequilibrium, while also capable of handling frozen flows. To represent the wedge computationally required the generation of a mesh. The CAD representation of the wedge was imported into the commercial meshing software, Pointwise® (now Cadence®). Given the flow conditions, the shock angle was approximated using compressible flow equations in the NACA 1135 Report shown in Ref. [23]. This angle with a slight uncertainty margin represented the outer domain of the computational mesh. After the computational domain was established, a 2-D mesh was generated. Given the simplicity of the geometry, a single block topology was created with 420 nodes in the streamwise direction and 150 nodes in the wall normal direction. The streamwise nodes were spaced tightly in the stagnation region to capture the small blunt nose of the plate. The wall normal spacing used a hyperbolic tangent distribution with the first cell height set to 1×10^{-7} meters. All turbulent results have Y+ globally less than 1. As US3D is a 3-D code, the mesh was extruded to be one cell thick. The baseline grid was coarsened and refined globally by a factor of 1.5. For the turbulent cases, the maximum heat-flux showed a difference of less than 3% between the medium and fine grids.

The US3D simulations solved the compressible Reynolds-averaged Navier-Stokes (RANS) equations with a single temperature and species model. US3D used a second-order in space Modified Steger-Warming inviscid flux scheme with DPLR implicit time integration to drive the problem to a steady state. The curved inlet of the domain was assigned a Dirchlet boundary condition based on the primitive values taken from the wind tunnel experiments. The side boundary conditions were made as slip walls, the wall was set to be a viscous isothermal wall at 350 K, and the outlet was set to be an extrapolation boundary condition. The aforementioned settings allowed for the simulation to drop the initial density residual by 12 orders of magnitude to achieve iterative convergence. The laminar cases applied no turbulence models while the turbulent cases used the Spalart-Allmaras (SA) model [24]. The SA model is an industry standard for modeling turbulence on external aerodynamic applications and has a long legacy of use [25]. While RANS models have significant uncertainty in hypersonic applications [26], their use is a standard practice in industry and academia [25].

D. Nitric Oxide Injection System

Introduction of nitric oxide was optimized to minimize flow perturbations and maximize NO concentration in the probe region above the test article. A seeder was designed to introduce NO into the preexpansion region. Introducing the NO at this upstream location allowed the seeded gas to mix with the bulk flow. Additionally, at this upstream location there was a series of aerogrids that mitigate the turbulence and wake structures formed within the bulk flow motion as well as during the NO seeding process. The seeder used for the present study was a 0.95 cm airfoil-shaped stainless-steel tube with a single 0.16 cm diameter orifice at a 6.7 cm height from the settling chamber floor. The relative position of the single orifice resulted in a reasonably uniform localized NO distribution above the test article. Additional information on the design of the seeder can be found in Refs. [21, 22, 27].

The measurements employed a gas mixture of 0.5% NO in nitrogen (N_2) via a continuous choked flow through the

seeder. The mixture was prepared before the experimental run in a pair of 3785 cm^3 stainless-steel ballasts upstream of the seeding location. Prior to mixing the gases, the system was evacuated with a Leybold D65B backing pump. The NO (99.95%, Praxair) in N_2 (99.999%, Brazos Valley Welding Supply) mixture was made by using a LabVIEW Proportional-Integral-Derivative (PID) algorithm. The PID algorithm was monitored by a pressure-dependent DC voltage output of a pressure transducer (Omega Type PX309-200A5V). The monitoring of the mixture pressure produced a pressure dependent DC voltage output to control mass flow controllers (MKS Mass-Flo 1179A) driven by a four-channel power supply/readout (MKS 247) operating at a set flow ratio. Gas mixtures of 9.3×10^3 Torr were made for each run by first filling the ballasts with nitric oxide to the predetermined partial pressure setpoint prior to filling the remaining volume with nitrogen.

E. PLIF System

Two PLIF laser systems generated output in the tunable 223 nm to 227 nm range for NO excitation using the $A^2\Sigma^+$ $(v' = 0) \leftarrow X^2\Pi$ $(v'' = 0)$ transition. The 223 nm to 227 nm light was generated by pumping a Sirah Cobra Stretch pulsed dye laser with the 532 nm second harmonic output of a Spectra-Physics PRO-290-10 Nd: YAG. The dye laser used a solution of Rhodamine 640 in ethanol to have output tunability from 600 nm to 630 nm. The residual 355 nm light from the PRO-290-10 Nd:YAG laser was mixed with the dye laser tunable output in a Sirah SFM-355-frequency mixing unit to produce 1 to 2.5 mJ per pulse in a range of 223 nm to 227 nm with a linewidth of 0.08 cm^{-1}.

The two UV beams were directed through a cylindrical lens array to produce two 1.5 cm wide 800 μm thick laser sheets and focused at the spanwise center of the model just above the surface as seen in Figure 3. The sheeted beams propagated from the top of the test section through the bottom via two mounted UV-grade fused silica windows. The beam entry orientation was necessary to establish the spatial distribution of NO along the streamwise direction of the test article. The resulting NO fluorescence was captured and spatially resolved using two PI-MAX4 ICCD cameras mounted perpendicular to the laser propagation on opposite sides of the ACE test section. Each camera was fitted with CERCO 100 mm F/2.8 UV lenses with 12 mm and 20 mm Kenko extension tubes to adjust the field of view and spatially aligned using a gridcard with a 1 mm $\times$ 1 mm grid. Each image was 2×2 binned to provide a camera resolution of 103 μm/pixel and the image acquisition rate was set to 10 Hz to synchronize with the 10 Hz Nd:YAG laser repetition rate. The images were specifically triggered following the laser scattering event from the surface of the UV window to increase the NO fluorescence signal. The time delay between the cameras was typically $\Delta t \approx 500$ ns each with gates of $20 - 40$ ns. A LabVIEW program was written to initiate image acquisition following an ACE facility pressure threshold to ensure correlation between the fluorescence images to the test section conditions such as stagnation temperature, static pressure, and Mach number.

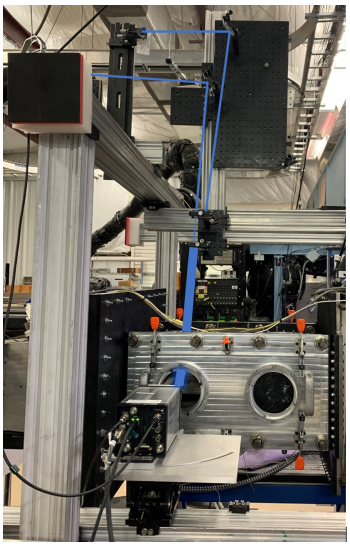

Fig. 3 PLIF thermometry setup. Only one laser beam is shown beyond the focusing optic for clarity. From Ref. [22], reprinted with permission.

F. Data Reduction

The rotational temperature measurements were performed using the two rovibronic transitions of the $A^2\Sigma^+$ (v' = 0) ← $X^2\Pi$ (v" = 0) vibrational band of nitric oxide, Q_{21}/R_1 J 1.5 and Q_{21}/R_1 J 8.5. The transitions were selected for the target temperature range of 60 – 350 K to ensure the population fraction of the high rotational state, J 8.5, would be sufficiently populated to yield ample fluorescence signal while ensuring temperature sensitivity. The sensitivity of the temperature measurements is given by Equation 1 [28],

$$\frac{\delta T}{T} = \frac{k_B T_{rot}}{\Delta E_{12}} \frac{\delta R_{12}}{R_{12}} \tag{1}$$

where δT is the temperature uncertainty, k_B is the Boltzmann constant, ΔE_{12} is the difference in energy calculated using the Dunham expansion, T_{rot} is the rotational temperature in Kelvin and δR_{12} is the ratio between the NO fluorescence images of the two transitions [8, 28]. According to Equation 1, the sensitivity of the temperature measurements is dependent on maximizing the energy difference between the probed rotational states while remaining in the population boundaries of the temperature range as the temperature uncertainty δT scales inversely proportional to ΔE_{12}. Spectroscopically isolated transitions were chosen to further minimize the uncertainty [29–31].

Prior to the temperature analysis, all fluorescence images were smoothed using a Fast Fourier Transform (FFT) function following background subtraction as shown in Equation 2,

$$X_{FFT} = FFT^{-1}\left(EXP\left(-\frac{(R_i - R_T)^2 + (C_j + C_T)^2}{w}\right) FFT\left(X_{ij}\right)\right) \tag{2}$$

where R_i is the row index, C_j is the column index, R_T is the image row resolution, C_T is the image column resolution, w is the weighting variable (user adjusted), and X_{ij} is the pixel value. The image blurring function reduced the degree of spurious temperatures produced from the temperature analysis. The final blurring was on the order of $4-5$ pixels, which correlated to a spatial blurring of $400-500$ μm, which was less than the size of the optically observable turbulence structures (*vide infra*) that were order $1-2$ mm.

For each image pair, the ratio of the two NO fluorescence images was determined in order to quantify the rotational temperature using Equation 3,

$$R_{12} = \frac{S_1}{S_2} = C_{12} e^{\left(-\frac{\Delta E_{21}}{k_B T}\right)} \tag{3}$$

where S_1 is the signal from the J 1.5 image, S_2 is the signal from the J 8.5 image, C_{12} is an empirical constant, ΔE_{21} is the energy difference between the two rovibrational states calculated using the Dunham expansion (2.56×10^{-21} J), k_B is the Boltzmann constant, and T is the temperature in Kelvin. Each column had its own unique C_{12} constant determined by using Equation 3 in the known freestream temperature region along the angle of the oblique shock. The freestream temperature was acquired by using the ratio of a pitot pressure in the settling region to a static pressure probe at the interface of the nozzle and test section to find the Mach number and relating the Mach number to temperature [23]. The C_{12} constants were determined using a dynamic region of interest (ROI) along the angle of the oblique shock defined by the user. Following the determination of the C_{12} constants, the rotational temperature for each pixel was determined using Equation 3 resulting in a 2-D temperature map as seen in Figures 6(a) and 6(b); this figure will be discussed in detail shortly. Lower and upper temperature bounds were set at 50 and 375 K, respectively, to filter nonphysical temperatures. To reduce the number of spurious temperatures from the final data set, temperature values outside a predefined 2σ statistical distribution were not accounted for in the final image data set. The statistically filtered set of temperature maps was then analyzed once more with the same process prior to taking the average of the instantaneous temperature maps as shown in Figures 6(a) and 6(b). Following the 2σ statistical treatment, greater than 85% of the determined freestream temperature values were accepted, however, up to 50% of the temperature values were discarded within 1 mm of the surface. The number of accepted values near the surface decreased due to an increase in scattering off the surface and the low signal due to the comparatively low number density near the hot wall.

For both laminar and turbulent temperature maps, the RMS of the fluctuations $T' = T - \overline{T}$ was calculated to quantify the turbulence intensity; $\overline{T'}$ could not be provided because it was by definition zero, a result confirmed from the data. When collapsing the 2-D temperature and fluctuation maps into 1-D profiles, the standard deviation of each row of data provided error bars and an estimate of the uncertainty. Because this resulted in taking an average of an average, the uncertainty produced was expected to be conservative. Further development of the uncertainty is an area of future work.

III. Results and Discussion

NO fluorescence images spanning 40 mm in the streamwise direction were collected at two different locations along the test article: an upstream location centered at 120 mm and a downstream location centered at 405 mm. Figure 4(a) is an average of the NO fluorescence images from the $A^2\Sigma^+$ (v' = 0) $\leftarrow$ $X^2\Pi$ (v" = 0) Q_{21}/R_1 J 1.5 transition and Figure 4(b) is an average of the NO fluorescence images from the $A^2\Sigma^+$ (v' = 0) $\leftarrow$ $X^2\Pi$ (v" = 0) Q_{21}/R_1 J 8.5 transition at the upstream location; each figure is an average of ~200 instantaneous laser power-corrected images collected during a single run. The higher intensity in Figure 4(b) relative to 4(a) is due to the 1.3:1 population ratio at 150 K. The fluorescence signal for both images gradually decreases toward the surface due to the local number density decreasing as a function of the increasing temperature and constant pressure normal to the plate. Using the higher rotational state J 8.5 addressed this challenge.

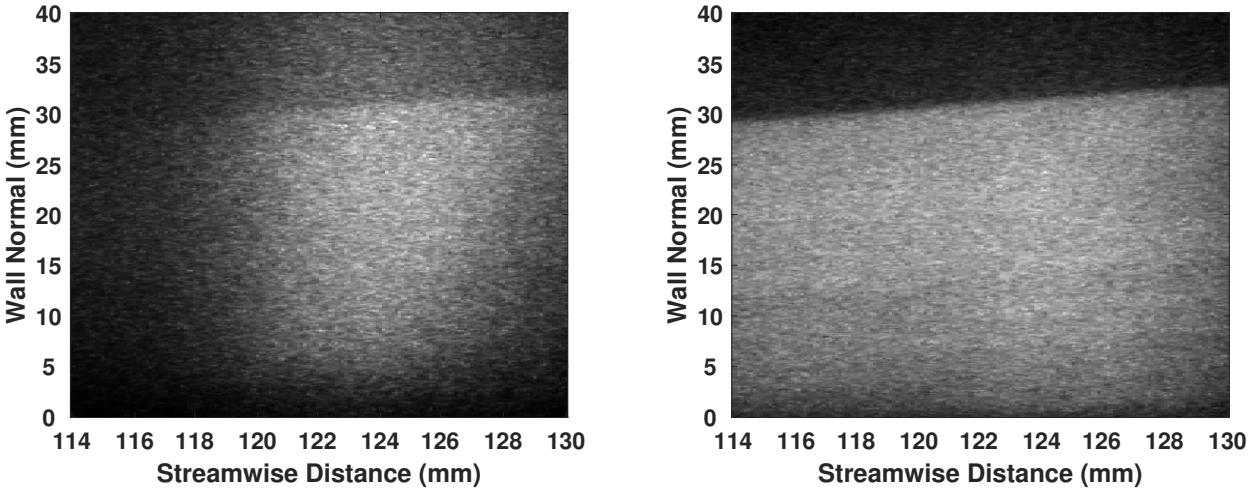

(a) J 1.5 transition

(b) J 8.5 transition

Fig. 4 Instantaneous raw streamwise NO fluorescence images for the laminar upstream location.

In both Figures 4(a) and 4(b), the strong discontinuity in the fluorescence signal at ~30 mm normal to the surface is attributed to the oblique shock produced from the leading edge of the test article. The increase in signal intensity across the shock is attributed to an increase in the static pressure, temperature, and local number density. Following oblique shock theory (see Ref. [23]), the static pressure beneath the oblique shock was expected to increase 45% (4.8 Torr) relative to the freestream pressure. Additionally, there were several weak Mach waves emanating from multiple forward/backward steps along the model due to the PEEK insert, laminar insert, two copper electrodes, and window insert upstream of the probed region. Due to the weakness of these Mach waves, the local number density rise across these shocks was difficult to estimate, but any effect on the results will be discussed when relevant.

Neither the higher rotational population nor the Mach waves may entirely account for the observed signal intensity of Figure 4(b). An alternative explanation may be multiple photochemical reactions occurring on the same timescale

as the PLIF measurement. The ACE tunnel operating conditions for this campaign yielded various nascent N_xO_y species with NO_2 and N_2O_3 being the predominant two species. Several studies have observed the NO photofragments produced from NO_2 and N_2O_3 UV photodissociation pathways yield nonstatistical rovibrational distributions [32–35]. The proposed reaction pathways for these nascent species are capable of producing rotationally excited NO $X^2\Pi$ (v = 0). Additionally, it has been shown at temperatures characteristic of expansion in the ACE tunnel that NO+O_2 can react exothermally to produce NO_2 [36]. Therefore, the observed fluorescence intensity for the J 8.5 image may be due to local photochemical perturbations produced by the NO laser diagnostic or otherwise elevated temperatures due to the formation of undesirable chemical products. The total effect of these reactions is significant but difficult to quantify, and it remains under investigation.

Concurrent with the laminar measurements, trips were inserted into the test article to induce turbulent flow, which is visualized in Figure 5. As in the laminar case, Figures 5(a) and 5(b) are images of the $A^2\Sigma^+$ (v' = 0) $\leftarrow$ $X^2\Pi$ (v" = 0) Q_{21}/R_1 J 1.5 transition and $A^2\Sigma^+$ (v' = 0) $\leftarrow$ $X^2\Pi$ (v" = 0) Q_{21}/R_1 J 8.5 transition, respectively. Here, however, the images are centered at 405 mm from the leading edge and instantaneous, single-shot images are shown to demonstrate the turbulent structures now present in the boundary layer. Tripped thermometry measurements performed at the upstream location are not presented for brevity.

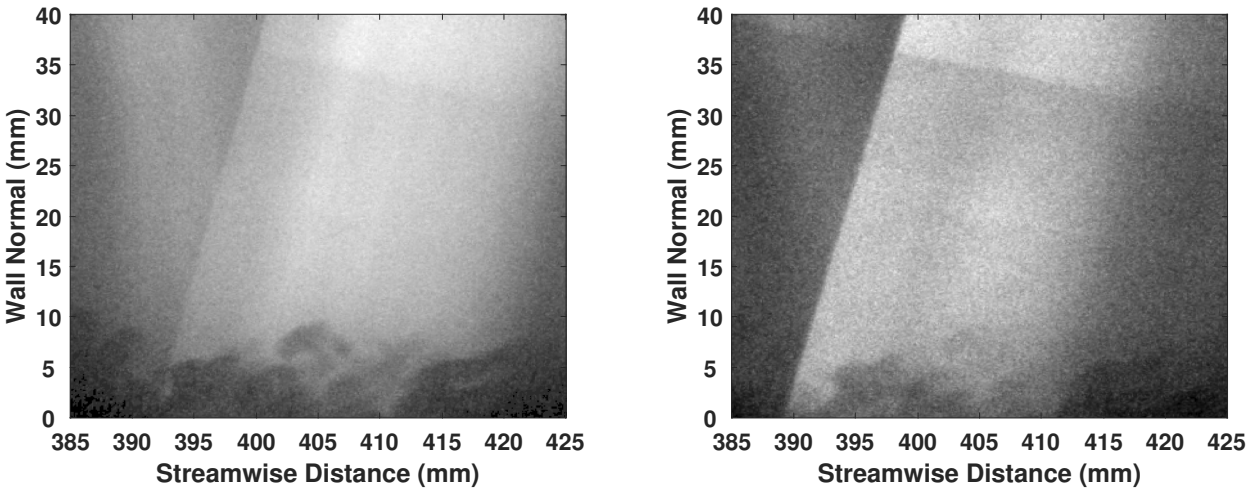

(a) J 1.5 transition

(b) J 8.5 transition

Fig. 5 Instantaneous raw streamwise NO fluorescence images for the turbulent downstream location.

Figures 5(a) and 5(b) show spatially and temporally resolved turbulence structures resulting from both the counter-rotating vortices emanating from the trip corners and also the wakes due to their obstructing of the flow [5]. From visual inspection, classical turbulence structures (chaotic appearance, entrained eddies, varying length scales, superlayer, etc.) were present. A reflected shock angled downward toward the test article was visible starting 40 mm normal to the surface, the origin being a <2 mm backward-facing step between the interface of the nozzle and the test section. Due

to this shock structure, the thermometry measurements were carefully selected to be conducted at 405 mm from the leading edge to ensure the freestream temperature used to scale the temperatures was unaffected. Also present from approximately 385 – 390 mm is fluorescence due to the reflected laser sheet.

Laminar and turbulent 2-D temperature maps at the upstream test location are shown in Figures 6(a) and 6(b), respectively. They were truncated to a 6 mm field of view due to the optimal laser overlap and minimized laser inhomogeneities within this region. In order to compare to computational boundary layer models, the temperature maps were horizontally averaged to produce the 1-D temperature profiles as seen in Figure 6(c). As the horizontal averaging spanned less than 1 cm, the boundary layer growth was assumed to be negligible over this distance. The corresponding fluctuation profiles are shown in Figure 6(d).

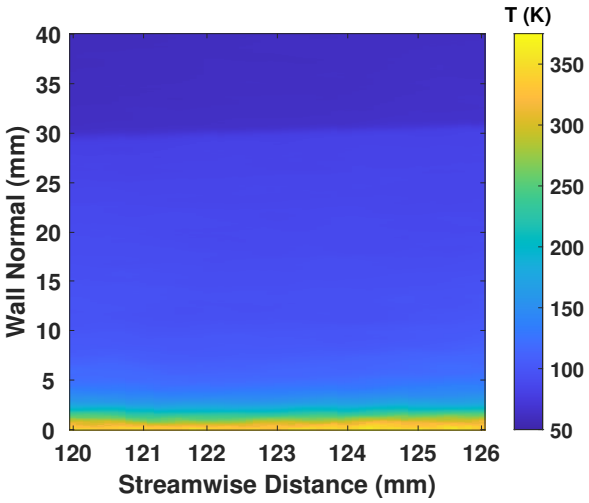

(a) Average laminar temperature map

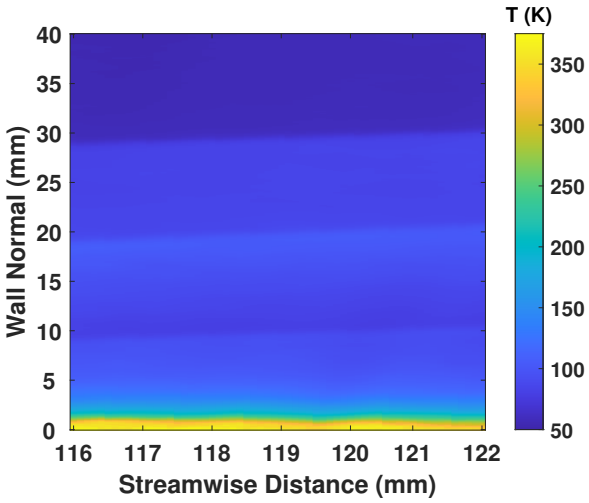

(b) Average turbulent temperature map

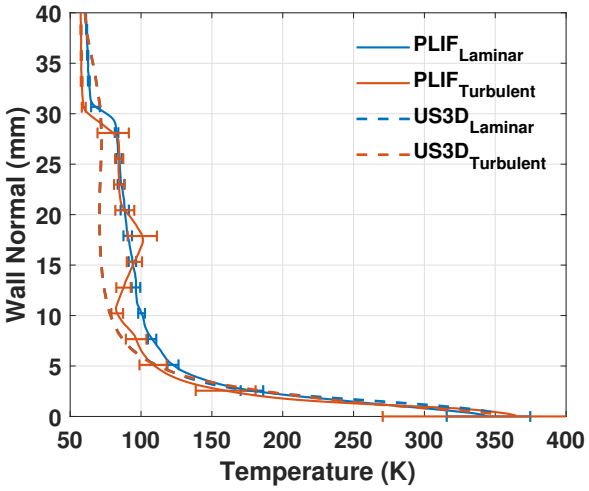

(c) Average temperature profiles for the upstream location

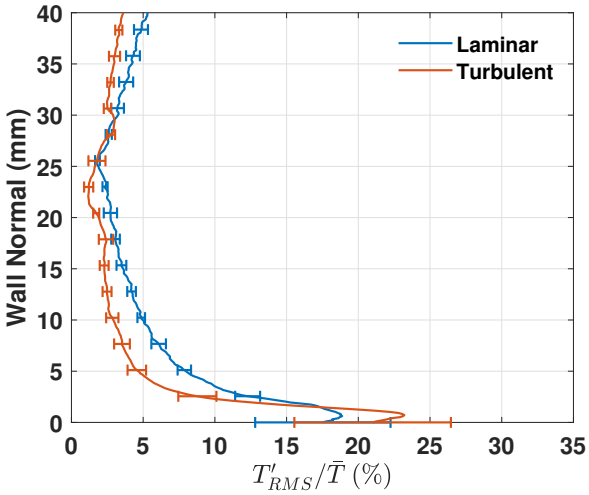

(d) Temperature fluctuation profiles for the upstream location

Fig. 6 Upstream average temperature maps and profiles for laminar and turbulent conditions.

The bow shock previously discussed manifests as a sudden temperature jump approximately 30 mm above the surface; in the profile plots it appears as a broadened, continuous rise due to the horizontal averaging [1]. The ROI chosen to determine the C_{12} constants was underneath the bow shock due to the larger signal in this region. The temperature of the ROI was adjusted until the determined freestream temperature was 58 ± 2 K. Using the oblique shock angle equations the temperature change across an oblique shock was expected to be 12% of the freestream temperature for an ideal gas at Mach 5.7 [23]. However, the temperature increase across the shock was found to be 83 K, a 30% increase in temperature. The observed discrepancy between the temperature measurement and the oblique shock calculations are attributed to the photodissociation pathways discussed previously; other potential explanations include nonuniform NO seeding leading to a spatially inhomogeneous N_xO_y distribution and deviation from oblique shock theory due to shock curvature. A major motivation for seeding into the settling chamber was to improve spatial uniformity of the seeded gas as well as to ensure full thermalization of the NO with the bath gas. These data suggest further analysis of additional chemical and photochemical processes are needed before this approach matches the expected theory.

The addition of the trips added two more shocks to Figure 6(b), a separation/reattachment shock at ~20 mm and a shear layer at ~10 mm due to the counterrotating vortices induced by the trips exchanging hot fluid from the wall with cold air from the freestream [5]. These features dominated the weaker Mach waves. The decrease in temperature below the trip separation/reattachment shocks was attributed to the expansion as the flow turned post-shock to travel along the wall [1].

For the laminar case, the results in Figure 6(c) show poor agreement with the computational results just below the bow shock, overpredicting the theory by ~15 K. However, below ~5 mm, the agreement improves until there is excellent overlap near the wall. Note that the PLIF data were not scaled to reach ~350 K at the wall, this was the result from the aforementioned post-shock calibration; this wall temperature was validated by taping a thermocouple to the glass surface during a run and by infrared thermography measurements on the PEEK insert. The large uncertainty near the wall was due to the low signal and high reflections in this region; again, the number of accepted values in the freestream was >85%, which decreased to 40 – 50%. The temperature rise beginning at ~5 mm from the wall was attributed to the entropy layer due to shock curvature from the blunted leading edge of the test article (see Ref. [21]), a feature corroborated by the computations. Fedorov and Tumin [37] determined the growing entropy layer has the potential to introduce velocity and temperature gradients, which can convolute with the boundary layer forming along the body. The thermal distinction between the entropy and boundary layers was difficult to discern within the presented measurements.

The turbulent results in Figure 6(c) match those from the laminar profile, which suggested the flow was not in full turbulence equilibrium. In this case, the fluctuation profile in Figure 6(d) was more illustrative. In the boundary layer, the tripped case showed larger peak fluctuations than the laminar case; that the fluctuations peaked above the wall suggests the formation of a laminar sublayer, but the high uncertainties frustrate definitive conclusions. The fluctuation profile does, however, more clearly demarcate the edge of the tripped boundary layer than the mean temperature image due to

the gradual temperature rise though the trip shear layers. The freestream temperature fluctuations 40 mm normal to the surface were measured to be 3 – 5%, which provides adequate agreement with the 1.5% RMS freestream fluctuations previously reported in Ref. [20]. It was unclear why the laminar profile has larger freestream uncertainties than the tripped case in Figure 6(d), but this was likely due to the resolution of the technique itself. The local temperature fluctuation minimum 25 mm above the surface is attributed to the placement of the user defined ROI to determine the C_{12} constants. There was relatively modest change in the fluctuation profile moving across the strong bow shock.

An estimate of the turbulence fluctuations from the total fluctuation profile was determined by subtracting the laminar fluctuation profile from the total fluctuation profile and taking the modulus. As previously discussed, the upstream location was transitional rather than turbulent, however, the turbulent fluctuations were determined at this location to obtain a baseline for comparison to the downstream location. As expected, the freestream fluctuations were small, $1-5\%$, reaching a minimum of less than 1% in the region chosen for the C_{12} ROI. The transitional turbulence fluctuations reached a maximum just above the surface at ~14% before decreasing to 12% at the wall.

The results from the downstream location are shown in Figure 7. Neither the bow nor trip shocks are visible in either temperature maps (Figures 7(a) and 7(b)), though a weak Mach wave propagating toward the plate from ~35 mm is present; as discussed above, this propagated from the interface of the tunnel nozzle and test section. Due to the complex nature of the shock structures and the recovery observed in Figure 6(c), no correction for the effect of the trip shock structure on the freestream temperature was taken; the same post-bow shock temperature of 83 K was used for scaling the data as in the upstream location, and as expected the predicted wall temperature was the same reasonable 350 K.

The laminar temperature profile in Figure 7(c) is nearly identical to the profile at the upstream location. This is attributed to the convolution of the entropy layer with the thermal boundary layer. The exact self-similar solutions of van Driest [38] do not predict δ greater than the ~5 mm entropy layer even 405 mm from the leading edge, so the entropy layer should not have been swallowed. It seems the entropy layer dominated the temperature boundary layer, a feature not predicted by the US3D simulations, which overpredicted the size of the temperature profile by a factor of two. Neither the raw flow visualization data nor supplementary schlieren data (see Ref. [22]) of the laminar boundary layer at the downstream test location show any evidence of the boundary layer or entropy layer above 5 mm, though the latter does show more boundary layer growth than was observed here.

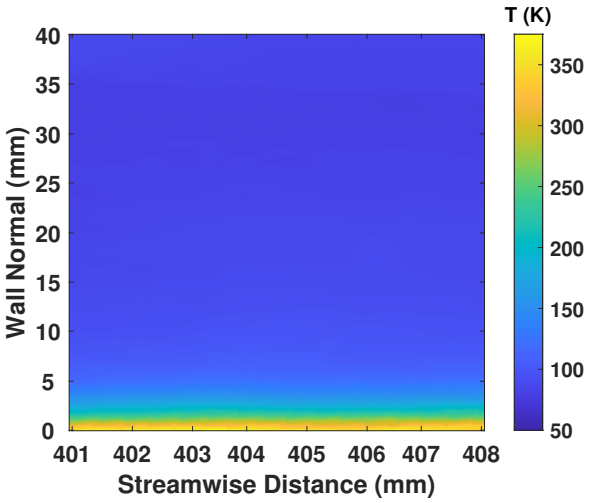

(a) Average laminar temperature map

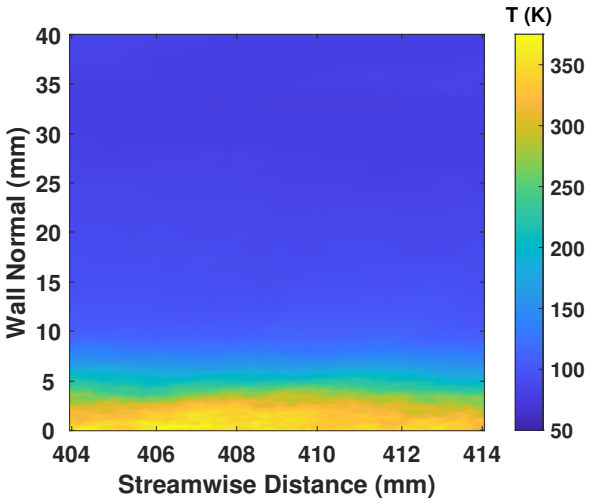

(b) Average turbulent temperature map

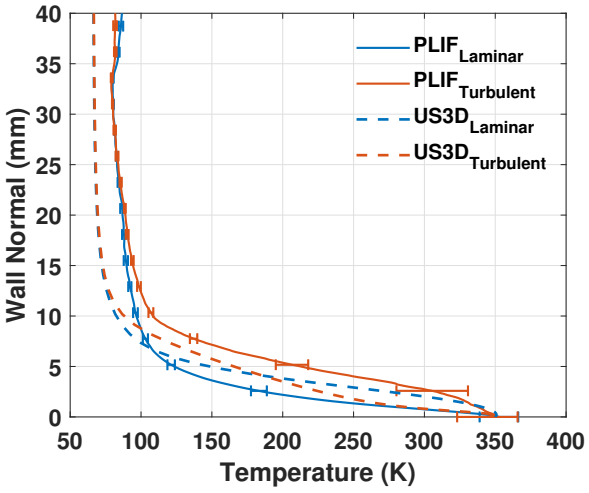

(c) Average temperature profiles for the downstream location

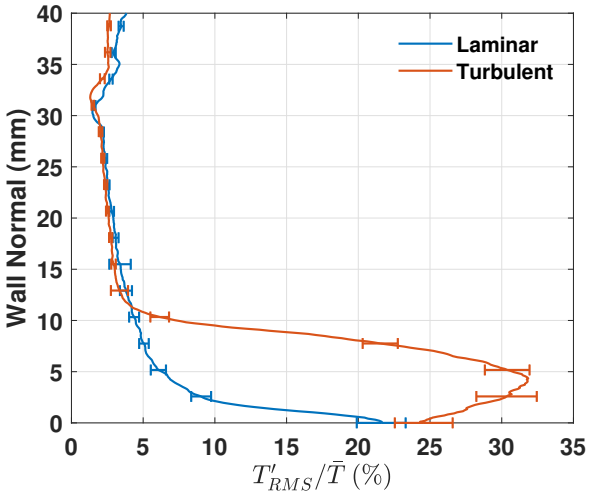

(d) Temperature fluctuations for the downstream location

Fig. 7 Downstream average temperature maps and profiles for laminar and turbulent conditions.

The turbulent data in Figure 7(c) did show significant growth between the upstream and downstream test locations likely because the boundary layer became fully turbulent. The height predicted matched the schlieren data in Ref. [22], and although $\delta_{PLIF} \approx \delta_{US3D}$, the temperatures measured through the boundary layer were now larger than the simulation. This may have been due to the higher than expected freestream temperature used to scale the PLIF temperatures, but another explanation could be that the simulation did not account for the full effect of the trips such as the wakes, separation/reattachment, vortical structures, etc. Here the uncertainty at the wall was less than in the upstream location, but this was likely due to fewer rejected images; away from the wall, the error bars between the two cases were comparable.

The fluctuation profiles in Figure 7(d) showed excellent agreement between the laminar and turbulent cases in the freestream. The freestream fluctuation of ~3% matched the results from Figure 6(d). The fluctuations in the downstream test location were a few percent lower through the boundary layer than those at the upstream test location everywhere except at the wall, perhaps due to the absence of the Mach waves present in the upstream location; the fluctuations at the wall were larger at the downstream test location, but this was because the results at the downstream location did not show the same trend reversal as was seen in the upstream case, a feature that could well be masked by the high uncertainty in this region in both cases. The turbulent profile showed the efficacy of the trips in generating turbulence as peak fluctuations exceeded 30%. As before, the fluctuation profile plot clearly demarcated the edge of the boundary layer, now at ~12.5 mm. Although the peak fluctuations at ~4 mm were too far from the wall to be attributed to the overlap region of the turbulent boundary layer, that the fluctuations were reduced almost by a third approaching the wall suggested the presence of a well-established laminar sublayer.

The process of estimating the turbulence fluctuations from the total fluctuation profile was repeated at the downstream location, which yielded more interesting results than the upstream location. Following the total fluctuation profile, the estimated turbulence fluctuations through the freestream and reflected shock are even smaller than the upstream location at $1-3\%$. The turbulence fluctuations increase as expected at the edge of the boundary layer, 12.5 mm normal to the surface. The turbulence fluctuations peak around 5 mm above the surface at ~30%, almost double the transitional turbulence fluctuations from the upstream location, before decreasing to ~12% at the wall. It is worth noting the turbulence fluctuation estimates from the upstream and downstream locations meet at ~12% at the wall indicating the lower limit of the technique has been reached.

IV. Conclusion

Laminar and turbulent rotational thermometry measurements of the hypersonic boundary layer of a 2.75° half-angle wedge using NO PLIF in the ACE blow-down wind tunnel have been presented. The measurements were taken at two locations along the wedge to characterize initial and developed boundary layer conditions. The horizontally-averaged measurements were compared to a RANS US3D solver with mixed results. The PLIF profiles and US3D models yielded favorable comparisons in the freestream and boundary layer at the upstream location, but fell short of producing a satisfactory match underneath the bow shock. Current hypotheses for the temperature discrepancy beneath the bow shock include nascent N_xO_y species being formed on the timescale of the experiments resulting in an increased temperature below the bow shock, the 500 ns timescale between the two rotational fluorescence images, and the method of calculating the correctional constant. Current studies are actively investigating the temperature discrepancy beneath the bow shock. These unexpected results should be considered before injecting NO into the settling chamber of a large scale blow-down hypersonic wind tunnel for thermometric measurements.

Upon comparison of the fluctuations and uncertainties in both laminar and turbulent conditions at the upstream and downstream locations, it was observed that the laminar fluctuations and uncertainties were lower than their turbulent counterparts, as anticipated. At the downstream location, the uncertainties for the laminar and turbulent cases met at the wall at around 23% leading to the conclusion that the limit of the PLIF technique was reached. The lower signal near the wall due to the density drop in conjunction with scatter off the wedge surface increased the fluctuations and uncertainty. It would be beneficial for future studies to test the optimal timing between capturing the NO fluorescence images of the two distinct rotational transitions. In addition, future studies will measure the temperature above and below the bow shock to verify the temperature and determine if the system is a single temperature or two-temperature system.

Acknowledgments

The authors gratefully acknowledge support for this work in part from a grant from the Department of Defense Office of the Under Secretary of Defense (Vannevar Bush Faculty Fellowship Grant Number N00014-18-1-3020). Its contents are solely the responsibility of the authors and do not necessarily represent the official views of Texas A&M University or the Department of Defense.

References

[1] O'Byrne, S., Danehy, P., and Houwing, A., "PLIF temperature and velocity distributions in laminar hypersonic flat-plate flow," *20th International Congress on Instrumentation in Aerospace Simulation Facilities, 2003. ICIASF'03.*, IEEE, 2003, pp. 136–147.

[2] Anderson, J. D., *Hypersonic and high temperature gas dynamics*, Aiaa, 2000.

[3] Schetz, J. A., and Bowersox, R. D., *Boundary layer analysis*, American Institute of Aeronautics and Astronautics, 2011.

[4] Dewey Jr, C. F., and Gross, J. F., "Exact similar solutions of the laminar boundary-layer equations," *Advances in heat transfer*, Vol. 4, Elsevier, 1967, pp. 317–446.

[5] Semper, M. T., and Bowersox, R. D., "Tripping of a hypersonic low-Reynolds-number boundary layer," *AIAA Journal*, Vol. 55, No. 3, 2017, pp. 808–817.

[6] Kostak, H., and Bowersox, R. D., "Hypersonic boundary layer off-body and surface measurements on the AFOSR BOLT geometry," *AIAA Scitech 2020 Forum*, 2020, p. 1043.

[7] Feng, D., Goldberg, B. M., Naphade, M., Shneider, M. N., and Miles, R. B., "A model study of filtered Rayleigh scattering sensitivity to pressure and temperature," *2018 AIAA Aerospace Sciences Meeting*, 2018, p. 2042.

[8] Hanson, R. K., "Planar laser-induced fluorescence imaging," *Journal of Quantitative Spectroscopy and Radiative Transfer*, Vol. 40, No. 3, 1988, pp. 343–362.

[9] Seitzman, J. M., Kychakoff, G., and Hanson, R. K., "Instantaneous temperature field measurements using planar laser-induced fluorescence," *Optics letters*, Vol. 10, No. 9, 1985, pp. 439–441.

[10] Palma, P., Mallinson, S., O'Byrne, S., Danehy, P., and Hillier, R., "Temperature measurements in a hypersonic boundary layer using planar laser-induced fluorescence," *AIAA journal*, Vol. 38, No. 9, 2000, pp. 1769–1772.

[11] Palmer, J., and Hanson, R., "Planar laser-induced fluorescence temperature measurements in free jet flows with vibrational nonequilibrium," *31st Aerospace Sciences Meeting*, 1993, p. 46.

[12] Bathel, B., Danehy, P., Inman, J., Alderfer, D., and Berry, S., "PLIF visualization of active control of hypersonic boundary layers using blowing," *26th AIAA Aerodynamic Measurement Technology and Ground Testing Conference*, 2008, p. 4266.

[13] Arisman, C., Johansen, C., Bathel, B., and Danehy, P., "Investigation of gas seeding for planar laser-induced fluorescence in hypersonic boundary layers," *AIAA Journal*, Vol. 53, No. 12, 2015, pp. 3637–3651.

[14] Danehy, P., Wilkes, J. A., Alderfer, D. W., Jones, S. B., Robbins, A., Patry, D., and Schwartz, R., "Planar laser-induced fluorescence (PLIF) investigation of hypersonic flowfields in a Mach 10 wind tunnel," *25th AIAA Aerodynamic Measurement Technology and Ground Testing Conference*, 2006, p. 3442.

[15] McDougall, C. C., Hinman, W. S., Johansen, C. T., Bathel, B. F., Inman, J. A., and Danehy, P. M., "Nitric oxide planar laser-induced fluorescence thermometry measurements in a hypersonic boundary layer," *2018 aerodynamic measurement technology and ground testing conference*, 2018, p. 3629.

[16] Nishihara, M., Takashima, K., Jiang, N., Lempert, W., Adamovich, I., Rich, J., Doraiswamy, S., and Candler, G., "Development of a Mach 5 nonequilibrium-flow wind tunnel," *AIAA journal*, Vol. 50, No. 10, 2012, pp. 2255–2267.

[17] Arisman, C., Johansen, C., Bathel, B., and Danehy, P., "Investigation of gas seeding for planar laser-induced fluorescence in hypersonic boundary layers," *AIAA Journal*, Vol. 53, No. 12, 2015, pp. 3637–3651.

[18] Candler, G. V., Johnson, H. B., Nompelis, I., Gidzak, V. M., Subbareddy, P. K., and Barnhardt, M., "Development of the US3D code for advanced compressible and reacting flow simulations," *53rd AIAA Aerospace Sciences Meeting*, 2015, p. 1893.

[19] Semper, M., Tichenor, N., Bowersox, R., Srinvasan, R., and North, S., "On the design and calibration of an actively controlled expansion hypersonic wind tunnel," *47th AIAA Aerospace Sciences Meeting including The New Horizons Forum and Aerospace Exposition*, 2009, p. 799.

[20] Semper, M., Pruski, B., and Bowersox, R., "Freestream turbulence measurements in a continuously variable hypersonic wind tunnel," *50th AIAA Aerospace Sciences Meeting including the New Horizons Forum and Aerospace Exposition*, 2012, p. 732.

[21] Buen, Z. D., Broslawski, C., Smotzer, M., Kuszynski, J. E., North, S., and Bowersox, R. D., "Towards Vibrationally Excited Nitric Oxide Monitoring (VENOM) in a Laminar, Hypersonic Boundary Layer," *AIAA Scitech 2020 Forum*, 2020, p. 1275.

[22] Broslawski, C. J., "The modeling and experimentation of hypersonic turbulent boundary layers with and without thermal nonequilibrium," Phd thesis, Texas A&M University, College Station, TX, August 2022.

[23] John, J. E., and Keith, T. G., *Gas Dynamics*, 3rd ed., Pearson Prentice-Hall, 2006.

[24] Spalart, P., and Allmaras, S., "A one-equation turbulence model for aerodynamic flows," *30th aerospace sciences meeting and exhibit*, 1992, p. 439.

[25] Smits, A. J., and Martin, M. P., "Turbulence in supersonic and hypersonic boundary layers," *IUTAM Symposium on One Hundred Years of Boundary Layer Research*, Springer, 2006, pp. 221–230.

[26] Aiken, T. T., Boyd, I. D., Duan, L., and Huang, J., "Assessment of Reynolds Averaged Navier-Stokes Models for a Hypersonic Cold-Wall Turbulent Boundary Layer," *AIAA SCITECH 2022 Forum*, 2022, p. 0586.

[27] Buen, Z. D., "Implementation of NO LIF diagnostics to characterize the role of thermal non-equilibrium within a hypersonic turbulent boundary layer," Phd thesis, Texas A&M University, College Station, TX, December 2021.

[28] Cattolica, R., "OH rotational temperature from two-line laser-excited fluorescence," *Applied optics*, Vol. 20, No. 7, 1981, pp. 1156–1166.

[29] Sánchez-González, R., Srinivasan, R., Bowersox, R. D., and North, S. W., "Simultaneous velocity and temperature measurements in gaseous flow fields using the VENOM technique," *Optics letters*, Vol. 36, No. 2, 2011, pp. 196–198.

[30] Sánchez-González, R., Bowersox, R. D., and North, S. W., "Simultaneous velocity and temperature measurements in gaseous flowfields using the vibrationally excited nitric oxide monitoring technique: a comprehensive study," *Applied optics*, Vol. 51, No. 9, 2012, pp. 1216–1228.

[31] Sánchez-González, R., Bowersox, R. D., and North, S. W., "Vibrationally excited NO tagging by NO (A 2 Σ+) fluorescence and quenching for simultaneous velocimetry and thermometry in gaseous flows," *Optics letters*, Vol. 39, No. 9, 2014, pp. 2771–2774.

[32] Thompson, B., Harteck, P., and Reeves Jr, R., "Ultraviolet absorption coefficients of co2, co, o2, h2o, n2o, nh3, no, so2, and ch4 between 1850 and 4000 a," *Journal of Geophysical Research*, Vol. 68, No. 24, 1963, pp. 6431–6436.

[33] Brouard, M., Cireasa, R., Clark, A., Preston, T., and Vallance, C., "The photodissociation dynamics of NO 2 at 308 nm and of NO 2 and N 2 O 4 at 226 nm," *The Journal of chemical physics*, Vol. 124, No. 6, 2006, p. 064309.

[34] Potter, A., Dribinski, V., Demyanenko, A., and Reisler, H., "Exit channel dynamics in the ultraviolet photodissociation of the NO dimer:(NO) 2→ NO (A 2 Σ+)+ NO (X 2 Π)," *The Journal of chemical physics*, Vol. 119, No. 14, 2003, pp. 7197–7205.

[35] Kajimoto, O., Honma, K., and Kobayashi, T., "Formation of electronically excited nitric oxide and energy partitioning in the 193-nm photolysis of the nitric oxide dimer," *The Journal of Physical Chemistry*, Vol. 89, No. 13, 1985, pp. 2725–2727.

[36] Arisman, C., and Johansen, C. T., "Nitric oxide chemistry effects in hypersonic boundary layers," *AIAA Journal*, Vol. 53, No. 12, 2015, pp. 3652–3660.

[37] Fedorov, A., and Tumin, A., "Evolution of disturbances in entropy layer on blunted plate in supersonic flow," *AIAA journal*, Vol. 42, No. 1, 2004, pp. 89–94.

[38] van Driest, E., "Investigation of laminar boundary layer in compressive fluids using the Crocco method," Technical Note TN-2597, National Advisory Committee for Aeronautics, Washington DC, January 1952.